Monte Carlo simulation of the generation of terahertz radiation in GaN

E. Starikov, P. Shiktorov, and V. Gružinskis
Semiconductor Physics Institute, A. Goštauto 11, 2600 Vilnius, Lithuania

L. Reggiani[a)]
Dipartimento di Ingegneria dell' Innovazione, Istituto Nazionale di Fisica della Materia, Università di Lecce, Via Arnesano s/n, 73100 Lecce, Italy

L. Varani and J. C. Vaissière
Centre d'Electronique et de Micro-optoélectronique de Montpellier (CNRS UMR 5507), Université Montpellier II, 34095 Montpellier Cedex 5, France

Jian H. Zhao
SiCLAB, Department of Electrical and Computer Engineering and CAIP Center, Rutgers University, Piscataway, New Jersey 08855

(Received 1 August 2000; accepted for publication 26 October 2000)

The conditions for microwave power generation at low temperatures under optical phonon emission are analyzed by Monte Carlo simulations of both small- and large-signal responses in bulk zinc blende and wurtzite GaN. As a result of the high optical phonon energy and the strong interaction of electrons with optical phonons in GaN a general improvement on the transit-time resonance and a considerable increase in the maximum generation frequency and power can be achieved in comparison to the widely studied III–V materials such as GaAs and InP. A dynamic negative differential mobility caused by transit-time resonance occurs in a wide frequency range of about 0.05–3 THz and persists in the THz frequency range up to the liquid nitrogen temperature with doping levels up to about $5\times10^{16}\,\mathrm{cm}^{-3}$. The efficiency of the amplification and generation is found to depend nonmonotonously on static and microwave electric field amplitudes, generation frequency, and doping level so that for each generation frequency there exists an optimal range of parameter values. Under optimal conditions a generation efficiency of about 1% to 2% can be achieved in the 0.5–1.5 THz frequency range. © 2001 American Institute of Physics.
[DOI: 10.1063/1.1334924]

I. INTRODUCTION

In the last decade, significant efforts have been devoted to searching for semiconductor sources of tunable THz radiation due to the strong interest in their possible applications in broadband communication, high-resolution spectroscopy, and radars, etc.[1] Indeed, the THz region represents a border range of frequencies of great interests for both basic and applied research. However, the intrinsic difficulty appearing here is that the bordering regions make use of quite different ways for radiation generation. From the low frequency side, it is the millimeter wave and microwave (MW) region ($f=30$–300 GHz or $\lambda=1$ cm–1 mm) where generation is usually obtained by starting from various current instabilities appearing in Gunn-devices, IMPATT, Schottky-diodes, etc., which are then placed in a waveguide resonant cavity. From the high frequency side, it is the infrared and optical region where generation is usually achieved by optical methods making use of the stimulated radiation coming from lasers. In each of these ways, the generation efficiency decreases significantly when trying to extend the generation into the THz region. Therefore to develop THz sources it becomes necessary either to exploit some new approaches and methods or to find new materials where some known mechanisms can lead to efficient power generation into the THz frequency range.

A lot of work has been done to push high power generation into the THz frequency range. For example, one way to approach THz power generation is to make use of various current instabilities in the transport of carriers in modern submicron and nanometric structures. The Gunn and IMPATT diodes which already work at frequencies of 100–200 GHz[2–4] can be considered as prototypes for this class of sources. To extend the power generation of these devices into the submillimeter and THz frequency range different possibilities have recently been proposed, including frequency mixing and multiplication in Schottky barrier diodes,[5] reduction of the transit time in deep submicron Gunn-oscillators,[6] resonant tunneling in double barrier heterostructures,[7] photon-assisted tunneling in resonant tunnelling diodes,[8] ballistic motion of carriers with negative effective-mass,[9] and various plasma instabilities.[10–12] However, in these devices an increase in the generation frequency is usually accompanied with both an increase in the required current density[4] and a decrease in the absolute value of the negative differential resistance. The former leads to an unacceptable increase in the device temperature while the latter results in a severe limitation on the generation frequency when the intrinsic negative differential resistance of the

[a)]Electronic mail: lino.reggiani@unile.it

 © 2001 American Institute of Physics

Downloaded 13 May 2001 to 128.113.4.240. Redistribution subject to AIP license or copyright, see http://ojps.aip.org/japo/japcr.jsp

structure becomes comparable to the device contact resistance.[13]

A second way to obtain THz generation is to exploit the ideas of quantum optical and lasing systems by making use of the concept of a population inversion in an active medium which can amplify propagating electromagnetic waves in the corresponding frequency range. In this case, the generation is obtained by the stimulated emission of radiation in the active semiconductor placed in a resonant system. The population inversion is usually created in complicated energy bands with carriers heated by external fields. For THz generation, the peculiarities of the valence band of most semiconductors are used. Here, due to degeneracy of the energy spectrum, light- and heavy-hole subbands are known to coincide at the center of the Brillouin zone so that direct optical transitions, corresponding to the desired frequency range, are possible at low hole energies of $\varepsilon(\mathbf{p}) < 40-50\,\mathrm{meV}$, with $\mathbf{p}$ the quasi-momentum. For example, in the case of *p*-type Ge at low temperatures with carriers heated by crossed electric and magnetic fields, population inversion of the interband and intraband transitions can be realized due to the combined action of several physical mechanisms including overpopulation of the light-hole subband, different shift and heating of the light and heavy holes (LHH), impurity scattering in the light-hole subband, Landau quantization, etc.[14] For this kind of THz generation, the hot-carrier interaction with the radiation has a pronounced resonant character inherent to carrier transitions between energetic states. This yields generation lines which are sufficiently narrow, and the possibility to control the generation frequency through external fields. The energy spectrum of the transitions, and hence of the stimulated radiation, can be additionally controlled in different ways through changing the field orientation in warped valence band, the uniaxial stress, and the Landau quantization. At present, following the aforementioned ideas, the LHH laser with a continuous tuning of the generation frequency in the 1–4 THz range has been realized.[15] It should be underlined that, due to the dispersion of the hole energy spectrum, population inversion of the LHH transitions persists up to very low frequencies. However, the so-called Drude absorption, i.e., radiation absorption by free carriers due to scattering events, inherent to this kind of devices completely dampens power generation at frequencies below 1 THz.[16]

The development of THz lasers demonstrates certain advantages of the second approach over the first approach. The idea of realizing a hot-carrier maser can be considered as a combination of the above two approaches. In the case of hot-carrier maser, similar to the THz laser, generation is obtained in the bulk semiconductor when the medium is active and can amplify propagating electromagnetic waves. However, the hot-carrier maser amplification, similar to that in the Gunn device is caused by a dynamic negative differential conductivity (DNDC) appearing in a narrow region of the high-frequency spectrum (see, for example, the transit-time resonance of hot electrons in momentum space,[17–20] the cyclotron resonance of holes with negative effective mass, etc.)[21,22] Usually, DNDC is related to the occurrence of ballistic carrier motion in some region of momentum space and the associated formation of needle-like distribution functions for charge carriers.

At present, the experimentally demonstrated heavy-hole cyclotron resonance NEMAG with a continuous tuning of the generation frequency in the millimeter wave range ($f = 40-330\,\mathrm{GHz}$)[21] can be considered as a representative of such a kind of generators. Theoretical estimations based on the Monte Carlo (MC) simulation show that similar conditions for MW amplification can be achieved in *n*-type InP due to optical phonon transit-time resonance (OPTTR).[18,19] A generation band of $f = 40-400\,\mathrm{GHz}$ with a maximum gain of about $200\ \mathrm{cm}^{-1}$ is predicted.[18,19] Just recently, millimeter wave generation caused by this effect was observed experimentally for the first time in *n*-type InP[20] under conditions predicted by MC calculations.[18,19] As a result, we can expect that the wide-gap semiconductors such as GaN and SiC be very promising materials for the development of high performance OPTTR masers because of the high value of the optical phonon energy and the strong interaction of electrons with polar optical phonons. The expected improvements would include an increase in the working temperature and the generation frequency.

The aim of this work is to investigate theoretically the conditions for OPTTR maser effects in GaN. Since these effects are caused by a quasiballistic heating of carriers under strongly nonequilibrium conditions, the theoretical analysis is carried out by using a MC method, which is known to provide a complete microscopic picture of carrier transport taking into account details of the band structure, scattering mechanisms, etc. Moreover, when considering hot-carrier effects in bulk materials subjected to constant or periodic electric fields, a single-particle procedure is usually sufficient if space-charge effects can be neglected. This is the case of hot-carrier lasers and masers, where the MC method is widely used and generally found to provide a good agreement with experimental data.[14–22]

The article is organized as follows. A qualitative description of the physics involved and the conditions necessary for the OPTTR is carried out in Sec. II. The MC procedure used to calculate the differential mobility spectrum under hot electron conditions is described in Sec. III. Section IV presents the numerical results of the linear response analysis based on the simulations. The results of the nonlinear analysis are presented in Sec. V. Finally, the main conclusions are drawn in Sec. VI.

II. GENERAL CONDITIONS FOR OPTTR

Let us consider in some detail the physical conditions leading to OPTTR. Due to the threshold characteristic of the optical phonon emission in bulk semiconductors at low lattice temperatures, the momentum space is conveniently subdivided into two regions characterized by low (passive) and high (active) intensities of carrier scattering. This situation is illustrated in Fig. 1, where the energy dependence of the main scattering rates in wurtzite GaN calculated at a lattice temperature of $T_0 = 10\,\mathrm{K}$ and with an ionized impurity concentration of $N_D = 10^{16}\,\mathrm{cm}^{-3}$ is shown. For acoustic and polar optical phonon scatterings the standard expressions are

Downloaded 13 May 2001 to 128.113.4.240. Redistribution subject to AIP license or copyright, see http://ojps.aip.org/japo/japcr.jsp

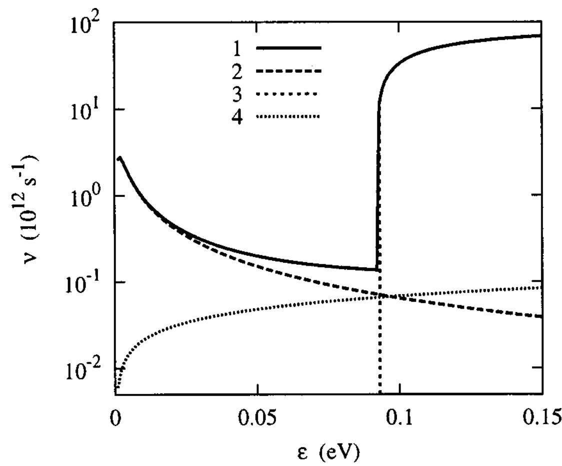

FIG. 1. Scattering rates in wurtzite GaN at $T_0 = 10$ K and $N_D = 10^{16}$ cm^{-3} as a function of carrier energy ϵ. Curves 1–4 correspond, respectively, to the scattering rates of total, impurity, polar optical phonon emission, and acoustic phonon.

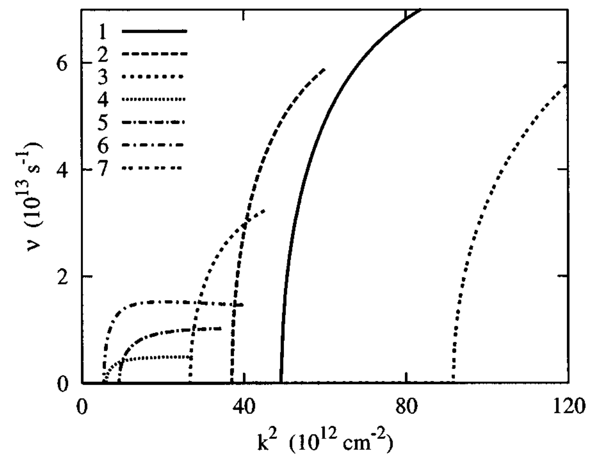

FIG. 2. Scattering rates due to polar optical phonon emission in wurtzite GaN, zinc blende GaN, InN, GaAs, InP, CdTe, and 4H-SiC (curves 1–7) as a function of squared wave vector at $T_0 = 10$ K.

used.[23] Note that due to the high value of the optical phonon energy, $\hbar\omega_0 = 92$ meV, being proportional to the occupation factor $[\exp(\hbar\omega_0/kT) - 1]^{-1}$, the probability of optical phonon absorption is practically negligible up to liquid nitrogen temperatures. The scattering rate by ionized impurity is calculated in the momentum relaxation time approximation of the Conwell–Weiskopf approach, and as is well-known it decreases sharply with increasing electron energies (curve 2). Accordingly, impurity scattering at low and intermediate doping levels occurs essentially at small values of electron momentum.

In the passive region, where the carrier energy $\varepsilon(\mathbf{p})$ is less than that of the optical phonon $\hbar\omega_0$, optical phonon emission is absent and only weak elastic scatterings caused by acoustic phonons and impurity ions are possible. The intensity of the momentum relaxation in this region is conveniently characterized by an average relaxation rate $\nu^- = \nu_{\text{imp}} + \nu_{\text{ac}}$ or by the corresponding average relaxation time $\tau^- = 1/\nu^-$. In the active region, where $\varepsilon(\mathbf{p}) > \hbar\omega_0$, the optical phonon emission with a characteristic time $\tau^+ \ll \tau^-$ plays a dominant role in the relaxation of both energy and momentum. Within a simple spherical and parabolic band, the boundary between passive and active regions is a sphere of radius $p_0 = (2m_0 m^* \hbar\omega_0)^{1/2}$, where m_0 is the free electron mass and m^* the effective mass of carrier. The threshold characteristic of the optical phonon emission rate determines most features of carrier heating in applied external fields.[14,24–28]

When a constant electric field E_0 is applied to a bulk semiconductor, the formation of a distribution function strongly elongated along the field direction (the so-called streaming) and the appearance of a cyclic dynamics for the single-carrier motion in momentum space are possible. For the streaming to be formed, the time of a ballistic free flight for a carrier moving from the centrum of the optical phonon sphere up to its boundary, $\tau_E = p_0/eE_0$, must satisfy the following conditions:

$$\tau^+ \ll \tau_E \ll \tau^-. \tag{1}$$

The condition of $\tau_E \gg \tau^+$ implies that the penetration into the active region is sufficiently small so that, after an optical emission, the carrier comes back near the center of the passive region, creating a sufficiently compact distribution (the so-called source). The condition of $\tau_E \ll \tau^-$ implies that, under the action of the electric field E_0, the source crosses the momentum space up to the boundary of the active region almost in the absence of scatterings. These conditions are conveniently rewritten in terms of lower and upper limits for the electric field magnitude as

$$\frac{p_0}{e\tau^-} \ll E \ll \frac{p_0}{e\tau^+}. \tag{2}$$

As T_0 and/or N_D increase, the characteristic time τ^- as well as the difference between τ^- and τ^+ decrease. This leads to a deterioration of the streaming conditions. Therefore materials with short τ^+ (i.e., with high upper limit for the electric field strength) are preferred.

Figure 2 presents the scattering rate of optical phonon emission for electronic wurtzite GaN, zinc blende GaN, InN, GaAs, InP, CdTe, and 4H-SiC (curves 1–7) as a function of the square of wave vector. It is evident that the conditions for streaming are superior in GaN than in other materials (with the exception of SiC).

When conditions (1) and (2) are satisfied, a carrier in the momentum space takes the well-known cyclic motion characterized by τ_E. The smaller the penetration into the active region is the closer the carrier moves to the cyclic trajectory. Such a cyclic motion is responsible for a number of effects, including transient velocity oscillations in a nonstationary state,[29] oscillations of the correlation function of velocity fluctuations and corresponding sharp peak of the spectral density of velocity fluctuations at the transit time frequency, $\nu_E = 1/\tau_E$, in a stationary state,[18,19,30] etc. In particular, these conditions were found[31–34] to favor the onset of high-frequency NDM which can arise in frequency regions near the resonant frequencies corresponding to the fundamental and higher harmonics of ν_E. For this reason, we introduce the dynamic NDM (DNDM) in contrast to the static NDM of the standard Gunn effect. The DNDM is associated with a

Downloaded 13 May 2001 to 128.113.4.240. Redistribution subject to AIP license or copyright, see http://ojps.aip.org/japo/japcr.jsp

modulation of the carrier distribution in the neighborhood of the cyclic trajectory. Such a modulation can result from both carrier penetration into the active region and weak scattering in the passive region.[31–34] In the latter case, the scattering mechanisms whose intensity decreases with the increase of carrier energy inside the passive region (e.g., impurity scattering, see curve 2 in Fig. 1) are the most favorable for the NDM to appear.

III. MONTE CARLO CALCULATIONS OF DIFFERENTIAL MOBILITY SPECTRUM

The most comprehensive approach to calculate the differential mobility spectrum of hot carriers in bulk semiconductors is based on the linear response formulation.[35,36] Let a constant homogeneous electric field E_0 be applied in the x direction. The differential mobility in the longitudinal direction $\mu_{xx}(\omega)$ at cyclic frequency $\omega=2\pi f$ is then obtained by Fourier transforming the linear response function of the longitudinal drift velocity $K_{xx}(s)$ as

$$\mu_{xx}(\omega)=e\int_0^\infty K_{xx}(s)\exp(-i\omega s)ds. \tag{3}$$

In turn, the linear response function can be written in the form of[35,36]

$$K_{xx}(s)=-\int \langle v_x(\mathbf{p},s)\rangle_P \frac{\partial}{\partial p_x} f_0(\mathbf{p})d\mathbf{p}. \tag{4}$$

Here e is the electron charge, $f_0(\mathbf{p})$ the hot-electron distribution function in steady state, and $\langle v_x(\mathbf{p},s)\rangle_P$ the conditional longitudinal velocity of an electron at time moment s with the electron at point $\mathbf{p}$ at $s=0$.

The advantage of this formulation is that the gradient in momentum space of the distribution function in Eq. (4), which is usually unknown for hot electron conditions, can be easily represented in terms of before- and after-scattering ensembles by rewriting the steady-state Boltzmann transport equation in the form of

$$\frac{\partial f_0}{\partial p_x}=\frac{1}{eE_0}[\varphi_a(\mathbf{p})-\varphi_b(\mathbf{p})], \tag{5}$$

where

$$\varphi_a(\mathbf{p})=\int W(\mathbf{p},\mathbf{p}')f_0(\mathbf{p}')d\mathbf{p}' \tag{6}$$

and

$$\varphi_b(\mathbf{p})=\nu(\mathbf{p})f_0(\mathbf{p}) \tag{7}$$

are the after- and before-scattering ensembles, respectively, henceforth shortly denoted as a- and b-ensembles. Here $W(\mathbf{p},\mathbf{p}')$ is the probability per unit time for a carrier to be scattered from state $\mathbf{p}'$ into state $\mathbf{p}$ due to all scattering mechanisms acting independently, and $\nu(\mathbf{p})=\int W(\mathbf{p}',\mathbf{p})d\mathbf{p}'$ the corresponding integrated scattering rate. Let us recall, that the a-ensemble gives the carrier distribution immediately after scattering, and the b-ensemble corresponds to the carrier distribution just before scattering. Thus in such a form the collision term of the Boltzmann equation determines completely the longitudinal gradient of the steady-state distribution function needed to calculate the linear response function of the longitudinal drift velocity in accordance with Eq. (4).

The substitution of Eq. (5) into Eq. (4) gives the longitudinal linear response function expression:

$$K_{xx}(s)=\frac{1}{eE_0}\int \langle v_x(\mathbf{p},s)\rangle_P[\varphi_b(\mathbf{p})-\varphi_a(\mathbf{p})]d\mathbf{p}. \tag{8}$$

To use Eq. (8) in the MC method, it is necessary to proceed with time averaging along the simulated trajectory $\mathbf{p}(t)$. In the framework of the single-particle procedure the simulated trajectory consists of a sequence of carrier free flights interrupted by scattering events. The flights in momentum space are described by the motion equation $\dot{\mathbf{p}}=eE_0$ and simulate the field term of the Boltzmann transport equation. Each flight starts from some point $\mathbf{p}_a$ in momentum space where the carrier appeared after the last scattering event. Each flight terminates in some point $\mathbf{p}_b$, where the next scattering event takes place. The scattering transfers the carrier into another point $\mathbf{p}_a'$ of momentum space from which the next free-flight starts. The whole set of $\mathbf{p}_b$ points corresponding to all free flights of the random trajectory $\mathbf{p}(t)$ simulates the before-scattering ensemble $\varphi_b(\mathbf{p})$. Accordingly, the whole set of $\mathbf{p}_a$ points simulates the after-scattering ensemble $\varphi_a(\mathbf{p})$.

In the framework of MC simulations, the averaging of the probable velocity over a carrier ensemble with a given distribution $\varphi(\mathbf{p})$ is equivalent to the transient drift velocity calculation by an ensemble MC method, which at $s=0$ is distributed in accordance with a given function $\varphi(\mathbf{p})$. For the a-ensemble such an approach is fully consistent with the single-particle MC simulation, since a set of single-carrier subhistories which start immediately after each scattering event can be considered as the necessary set of separate carrier histories in the ensemble averaging. Therefore the linear response function term corresponding to the a-ensemble can be written as

$$K_{xx}^a(s)=\frac{1}{eE_0T}\sum_{i=1}^{N} v_x(t_i+s), \tag{9}$$

where t_i corresponds to the time moments of the scattering events, T is the total time of the simulated trajectory $\mathbf{p}(t)$, and N is the total number of the scattering events occurred in the time interval $[0, T]$.

Direct substitution of Eq. (7) into Eq. (8) gives for the b-component of the linear response function the expression

$$K_{xx}^b(s)=\frac{1}{eE_0}\int \langle v_x(\mathbf{p},s)\rangle_P \nu(\mathbf{p})f_0(\mathbf{p})d\mathbf{p}. \tag{10}$$

This expression coincides in form with the general definition of the correlation function of dynamic quantities and can be rewritten in terms of time averaging in the usual form as

$$K_{xx}^b(s)=\frac{1}{eE_0(T-s)}\int_s^T \nu[\mathbf{p}(t-s)]v_x[\mathbf{p}(t)]dt. \tag{11}$$

This means that the total simulated trajectory (or history) $\mathbf{p}(t)$ of a trial particle contains the subhistories, which form the b-ensemble history, in implicit form. The time dependence of the carrier velocity $\mathbf{v}[\mathbf{p}(t)]$ determined at any time

Downloaded 13 May 2001 to 128.113.4.240. Redistribution subject to AIP license or copyright, see http://ojps.aip.org/japo/japcr.jsp

moment t and multiplied by the initial value of the total scattering rate $\nu(\mathbf{p})$ can be considered as a subhistory of the b-ensemble. Thus quite different algorithms are required to calculate the a- and b-components of the linear response function in this case.

Using the mean time of free flight, Eqs. (8), (9), and (11) are conveniently rewritten in the following way where each term has a clear physical meaning:

$$K_{xx}(s)=\frac{1}{eE_0\langle\tau\rangle}[\langle v_x(s)\rangle_b-\langle v_x(s)\rangle_a], \tag{12}$$

where

$$\langle v_x(s)\rangle_b=\frac{\langle\tau\rangle}{T-s}\int_s^T \nu[\mathbf{p}(t-s)]v_x[\mathbf{p}(t)]dt \tag{13}$$

and

$$\langle v_x(s)\rangle_a=\frac{1}{N}\sum_{i=1}^{N} v_x(t_i+s) \tag{14}$$

are the probable velocities for the b- and a-ensembles, respectively, $\langle\tau\rangle=T/N$ is the mean time of free flight, and the quantity $eE_0\langle\tau\rangle=\langle p\rangle_0$ can be considered as the mean free path in momentum space.

IV. LINEAR ANALYSIS (SMALL-SIGNAL RESPONSE)

The MC procedure described above is applied to calculate the longitudinal differential mobility spectra in bulk zinc blende and wurtzite GaN. The parameters of the band models are taken from Refs. 37 and 38. The scattering mechanism from ionized impurities has been numerically optimized to shorten the CPU time associated with the large number of small angle scatterings. Moreover, due to the essential role played by impurity scattering, three models of screening have been checked, namely: Conwell–Weiskopf, Brooks–Herring with the lattice temperature, and Brooks–Herring with the electron temperature determined by the average energy of electrons. At low doping levels ($N_d \leqslant 10^{15}\,\mathrm{cm}^{-3}$) all three models give the same result in a wide range of electric fields where runway from low-energy impurity scattering already takes place. With the increase of doping level, the most severe restrictions for the onset of OPTTR conditions are found in the Conwell–Weiskopf approximation. Therefore we present below only numerical results obtained under this approximation, since other models of screening will lead only to improve OPTTR conditions. For time averaging in accordance with Eqs. (13) and (14), usually a time interval of $T=2\times10^6$ ps is used. The main steps of the procedure are illustrated in Figs. 3–5 for wurtzite GaN with $N_D=2\times10^{15}\,\mathrm{cm}^{-3}$ at $T_0=10$ K. To better illustrate the features related to the dynamic characteristics of the carrier motion, this set of figures present the results calculated at a relatively small value of the electric field, namely, $E_0=1.2$ kV/cm. Here, carrier runaway from the intensive impurity scattering at low energies already takes place, but penetration into the active region is still small so that most of the carrier trajectories in the passive region are close to the cyclic trajectory. Under these conditions the b-ensemble is mainly located in the active region just after its boundary and

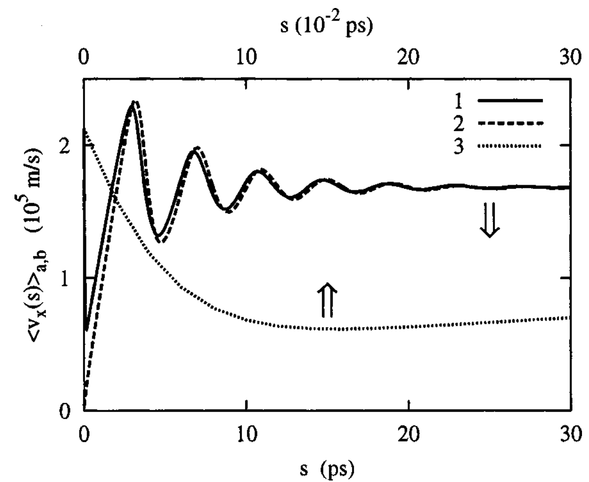

FIG. 3. Time dependences of the longitudinal velocities averaged over the before- and after-scattering ensembles, $\langle v_x(s)\rangle_b$ and $\langle v_x(s)\rangle_a$ (curves 1 and 2, respectively), calculated by the single-carrier MC procedure for wurtzite GaN at $E_0=1.2$ kV/cm, $T_0=10$ K, $N_D=2\times10^{15}\,\mathrm{cm}^{-3}$. Curve 3 shows the detailed initial stage of the relaxation of $\langle v_x(s)\rangle_b$ by using a time scale 100 times shorter than curves 1 and 2.

consists of electrons which are emitting optical phonons. Accordingly, the a-ensemble consists primarily of electrons which have just emitted optical phonons and is located near the center of the passive region slightly shifted towards positive values along the x axis due to the forward characteristic of the optical phonon emission.

Figure 3 shows the time dependences of the electron velocity averaged over the a- and b-ensembles, $\langle v_x(s)\rangle_a$ and $\langle v_x(s)\rangle_b$, respectively. Starting from a small positive value, $\langle v_x(s)\rangle_a$ corresponds to the average velocity of electrons just after scatterings and goes to dampened oscillations around the steady value of $\langle v_x\rangle_0$. Starting from a sufficiently high value, $\langle v_x(s)\rangle_b$ corresponds to the main location of the b-ensemble at the beginning of the active region. Due to the very quick emission of optical phonons in the active region,

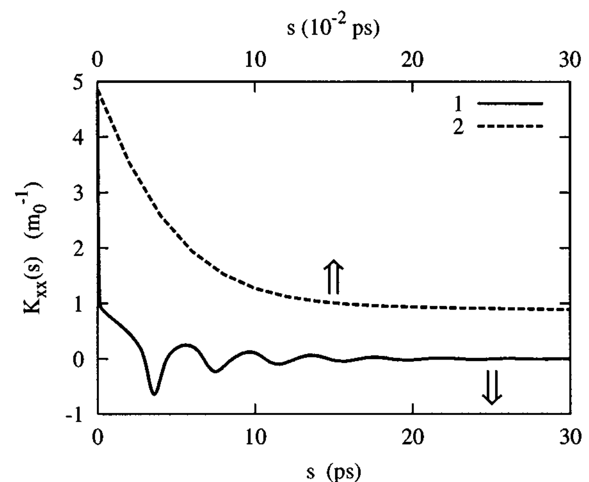

FIG. 4. Linear response function of the longitudinal velocity $K_{xx}(s)$ (curve 1) calculated by using Eq. (12) and the time-dependent velocities $\langle v_x(s)\rangle_b$ and $\langle v_x(s)\rangle_a$ presented in Fig. 3. Curve 2 shows the detailed initial stage of the relaxation of $K_{xx}(s)$ by using a time scale 100 times shorter than curve 1.

Downloaded 13 May 2001 to 128.113.4.240. Redistribution subject to AIP license or copyright, see http://ojps.aip.org/japo/japcr.jsp

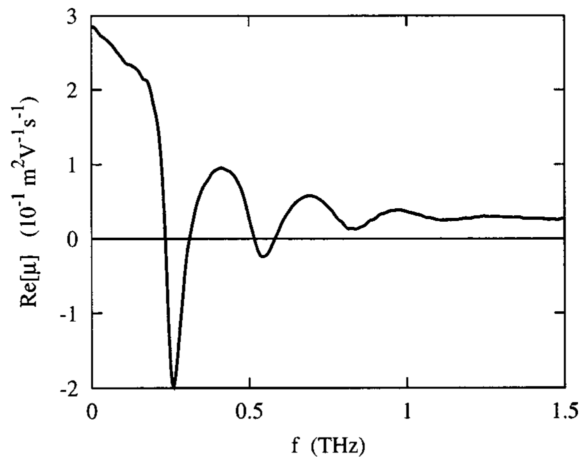

FIG. 5. Real part of differential mobility spectrum calculated by Fourier transform of the linear response function of the longitudinal velocity presented in Fig. 4. Negative values of Re[μ] correspond to the first and second amplification bands.

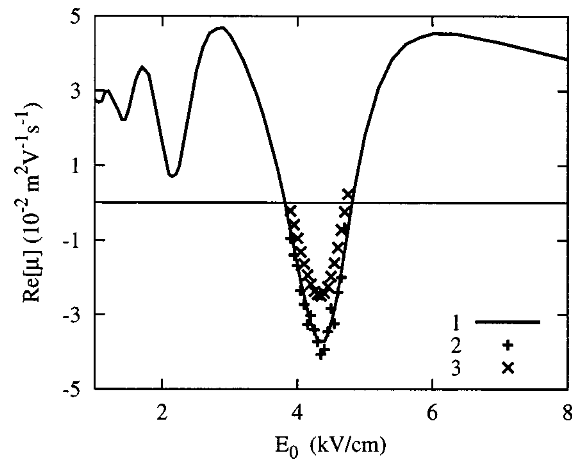

FIG. 6. Real part of the differential mobility at a frequency of 1 THz as a function of the static electric field strength for wurtzite GaN at $T_0 = 10$ K, $N_D = 10^{16}\,\mathrm{cm}^{-3}$ calculated by using: (i) the average over before- and after-scattering ensembles (curve 1) and (ii) the direct velocity response to the MW electric field with an amplitude of 0.2 kV/cm (curve 2) and 3 kV/cm (curve 3).

$\langle v_x(s)\rangle_b$ merges abruptly down to values corresponding to the *a*-ensemble. The stage of the initial rapid decrease of $\langle v_x(s)\rangle_b$ is shown in Fig. 3 by curve 3 which is plotted using a time scale 100 times shorter than that of curves 1 and 2. After the initial stage, $\langle v_x(s)\rangle_b$ also shows dampened oscillations around the stationary velocity. The damping of the oscillations of the *a*- and *b*-ensemble averaged velocities is connected with the gradual loss of coherence of the cyclic motion. This loss is caused by both the random scattering events in the passive region and the random penetrations into the active region. The two velocities approach the steady-state drift velocity $\langle v_x\rangle_0$ independent of each other. This guarantees that the linear response function, which in accordance with Eq. (12) is proportional to the difference between the above two velocities, tends to zero at long *s*.

The linear response function of the longitudinal drift velocity $K_{xx}(s)$ is presented in Fig. 4. This function starts from the value of the reciprocal effective mass $1/m^*$ and decreases abruptly due to the fall of the *b*-component. Again, this initial stage is shown more explicitly by curve 2 which is plotted using a time scale 100 times shorter than the main one. After the initial fast relaxation, $K_{xx}(s)$ exhibits damped oscillations aroud zero with a period $\tau_E \approx 4$ ps corresponding to a transit-time frequency $\nu_E = 1/\tau_E$ of about 250 GHz. Figure 4 clearly indicates the presence of some delay time before the starting of the damped oscillations. This implies a certain phase shift of the oscillations and leads to an anomalous resonant behavior of the longitudinal differential mobility which exhibits a series of minima at the transit-time frequency and its higher harmonics (see Fig. 5). For the case of the relatively small penetration presented in Figs. 3–5, the DNDM appears in the high-frequency region of the fundamental transit-time resonance and its second harmonic which correspond to the first and second amplification bands. Due to the resonant characteristics of the DNDM, each band is sufficiently narrow. The maximum values of the DNDM correspond to the optimal amplification frequencies f_{opt} in each band. Outside the amplification band, the positive differential mobility, and hence the absorption coefficient, exhibit reasonably high values. Such a behavior of the amplication and absorption spectra are preferable to achieving a single-mode generation. One can also distinguish the minima of Re[$\mu(f)$] at the third and the forth harmonics, however, their magnitude is insufficient to determine negative values of the differential mobility.

From the experimental point of view, it is often easier to fix a frequency (e.g., by taking a selective detector with maximum sensitivity in a very narrow frequency range) to investigate the absorption (or amplification) of the MW radiation as a function of the constant electric field applied to the sample. In this case, the resonant characteristic of the DNDM also manifests itself as a series of resonant peaks and minima. This behavior is illustrated in Fig. 6, which presents the field dependence of the real part of the differential mobility at a frequency of $f = 1$ THz calculated at $T_0 = 10$ K for wurtzite GaN with $N_D = 10^{16}\,\mathrm{cm}^{-3}$ (curve 1). Again, amplification is achieved in a narrow range of electric field. To check the accuracy of the differential mobility calculations and to illustrate the change in amplification at large MW field amplitudes, curves 2 and 3 show Re[μ] calculated directly from the velocity response to a harmonic MW field with an amplitude of $E_\omega = 0.2$ and 3 kV/cm, respectively. At small amplitudes the differential mobility calculated by the two procedures practically coincides (curve 2). At large amplitudes the mobility decreases monotonously in the whole amplification band and the amplification region becomes narrower (see the next section for a more detailed discussion concerning nonlinear effects).

Figure 7 summarizes the field dependence of the maximum negative value of Re[μ] for the first and second amplification bands for the zinc blende GaN sample with $N_D = 10^{15}\,\mathrm{cm}^{-3}$ (curves 1 and 2 in the lower part of the figure) and the amplification range for these bands [regions limited by curves 4–7 which show the lower (4,6) and upper (5,7) boundaries for the first (4,5) and second (6,7) bands in the upper part of the figure]. At low doping levels (N_D

Downloaded 13 May 2001 to 128.113.4.240. Redistribution subject to AIP license or copyright, see http://ojps.aip.org/japo/japcr.jsp

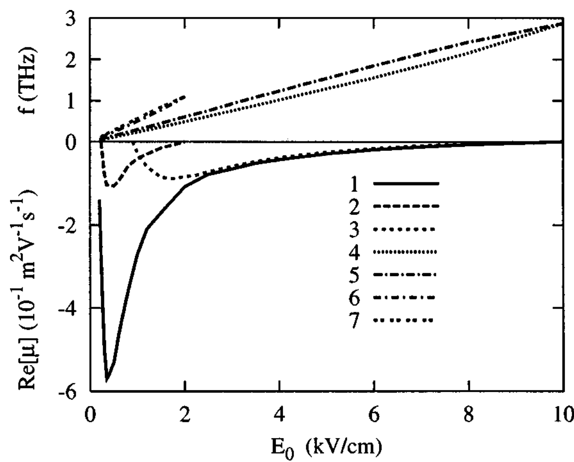

FIG. 7. Maximum values of the DNDM in the first and second amplification bands (curves 1 and 2) as well as lower (curves 4 and 6) and upper (curves 5 and 7) frequency limits of the amplification for the first (curves 4 and 5) and second (curves 6 and 7) bands calculated for zinc blende GaN as a function of the electric field E_0 at $T_0 = 10$ K and $N_D = 10^{15}$ cm^{-3}. The variation of the maximum value of the DNDM in the first amplification band with the increase in the doping level is illustrated by curve 3 calculated for $T_0 = 10$ K and $N_D = 10^{16}$ cm^{-3}.

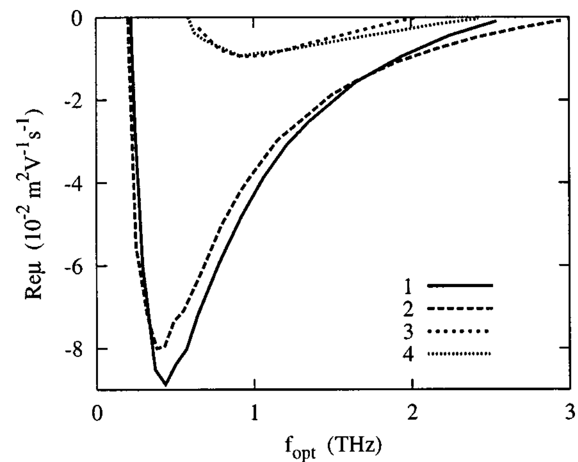

FIG. 8. Maximum values of the DNDM as a function of the optimal amplification frequency f_{opt} for zinc blende (curves 1, 3) and wurtzite (curves 2, 4) GaN samples with $N_D = 10^{16}$ cm^{-3} at $T_0 = 10$ (curves 1, 2) and 80 K (curves 3, 4).

$\leq 10^{15}$ cm^{-3}) the negative values of Re[$\mu(f)$] appear at sufficiently low electric fields $E_0 \approx 200$ V/cm and quickly reach the maximum values of the DNDM at $E_0 \approx 400$ V/cm. The appearance and rapid growth of the DNDM is connected with the electron runaway from the low-energy region dominated by impurity scattering and the formation of a needle-like distribution in momentum space. With a further increase in E_0 the maximum value of the DNDM decreases approximately as $1/E_0$ and finally the DNDM disappears at $E_0 \approx 10$ kV/cm due to a significant penetration of carriers into the active region, which destroys the coherence of successive free flights. The second amplification band exists only for a small penetration into the active region, i.e., in the low-field region (curve 2). Both the first and second amplification bands are very narrow (see curves 4, 5 and 6, 7), and the optimal amplification frequency corresponding to the maximum value of the DNDM in the band increases almost linearly with E_0, in full agreement with the expectation based on the simple expression for the transit-time resonance frequency given by $\nu_E = eE_0/p_0$. As evidenced by curves 4 and 5, at low doping levels, the amplification covers practically both millimeter and submillimeter wavelength ranges due to the appearance of the DNDM over a rather wide range of the electric field. With the increase of the doping level and, hence, the increase of the low-energy impurity scattering intensity, the threshold field for the onset of DNDM is shifted to higher values (see curve 3 which presents the maximum value of the DNDM in the first amplification band calculated for $N_D = 10^{16}$ cm^{-3}) due to the increase of τ^- in the right-hand side of Eq. (1). After the runaway from the impurity scattering has taken place, the curves for low and high impurity concentrations practically coincide, since further restrictions are primarily related to carrier penetration into the active region, and are similar for both low and high impurity concentration cases.

Analogous results are obtained for the wurtzite GaN. Due to the higher value of the effective mass ($m^* = 0.2$) with respect to that of zinc blende GaN ($m^* = 0.15$) the corresponding curves are slightly shifted (by about 20%) to higher field regions. Nevertheless, the dependence of the maximum value of the DNDM upon the optimal amplification frequency f_{opt} is quite similar in both cases as illustrated in Fig. 8. Here curves 1 and 2 are calculated at $T_0 = 10$ K for zinc blende and wurtzite GaN samples with $N_D = 10^{16}$ cm^{-3}. Curves 3 and 4 correspond to the same samples at $T_0 = 80$ K. With the increase of T_0 we observe that: (i) the frequency range of possible amplifications becomes narrower because of the narrowing of the electric field range which satisfies the conditions given by Eqs. (1) and (2), and (ii) the maximum values of the DNDM decreases. Nevertheless, amplification in the THz frequency range remains even at temperatures as high as around liquid nitrogen temperature. This is very important for many potential applications.

The investigation of the dependence of the amplification coefficient (gain) upon the doping level is of special interest and is presented below. In the region of DNDM the small-signal gain (i.e., the amplification coefficient in the absence of generation process) can be calculated as[14,39]

$$\alpha_0(f,n) = -\mathrm{Re}[\mu(f)]n\frac{e}{c\epsilon_0\sqrt{\epsilon}}, \tag{15}$$

where n is the free-carrier concentration, c the light velocity in vacuum, ϵ_0 the permittivity of vacuum, and ϵ the static dielectric constant of the material. We notice that DNDM depends crucially on carrier concentration. Therefore increasing doping concentration should increase the gain. However, increasing doping concentration also decreases the value of $-\mathrm{Re}[\mu(f)]$. The competition of these two opposite effects implies the existence of an optimum range of doping level where the gain is maximum. This observation is confirmed by our simulation results shown in Fig. 9, which presents the gain and the DNDM maximum values in the upper and lower parts of the figure, respectively, as a function of n

Downloaded 13 May 2001 to 128.113.4.240. Redistribution subject to AIP license or copyright, see http://ojps.aip.org/japo/japcr.jsp

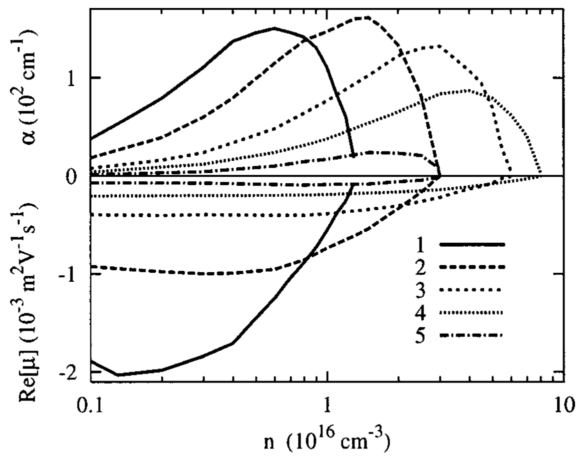

FIG. 9. Real part of differential mobility (lower curves) and gain (upper curves) as a function of electron concentration in wurtzite GaN at $T_0 = 10$ K for $f = 0.25$, 0.5, 1, and 1.5 THz (curves 1–4) and at $T_0 = 80$ K for $f = 1$ THz (curve 5).

at four fixed frequencies of $f = 0.25$, 0.5, 1, and 1.5 THz (curves 1–4) at $T_0 = 10$ K. To see the effect of increased temperature, curve 5 shows the results calculated for $f = 1$ THz at $T_0 = 80$ K. It is seen that both the gain and the DNDM persist at temperatures up to liquid nitrogen temperature although their magnitudes are reduced. As can be seen in Fig. 9, the possible maximum gain remains at about the same level around $\alpha = 100–150\ \mathrm{cm}^{-1}$ over a wide frequency range. However, the optimum doping level strongly depends on frequency and differs by as large as one order of magnitude.

V. NONLINEAR ANALYSIS (LARGE-SIGNAL RESPONSE)

In the previous section we have proved that GaN samples can be an active medium for THz frequency amplification under OPTTR conditions. To achieve THz generation it is necessary to put the active medium into a resonator system which must satisfy some conditions. The general situation can be qualitatively described as follows. In the presence of DNDM, an external resonant system will lead to the onset and increase of MW oscillations accompanied with an increase in the field amplitude of E_ω inside the sample. In the initial stage this increase will be accompanied with an increase in the MW power P_ω which, under small-signal conditions, is proportional to $\mathrm{Re}[\mu_\omega]E_\omega^2$. However, a considerable increase in E_ω will result in a decrease in the differential mobility and the associated dynamical gain. Finally, the complete disappearance of the amplification effect will take place when both the gain and the generated power will go down to zero. Therefore it becomes mandatory to choose the resonator characteristics and the output of the power generated by the sample in such a way so as to provide the maximum generated power inside the sample. The investigation of the conditions needed to obtain the maximum generated power and/or the maximum efficiency of THz power generation is one of the main tasks of nonlinear response analysis. To undertake this task, it is necessary to know the dependence of the generated power at the output of a resonator upon its generalized characteristics. Among the important parameters are the coupling coefficient of the active medium with the external free space, Γ, and the coefficient of internal losses inside the resonator, Λ. The internal losses are actually external losses with respect to the hot-carrier system. For example, in the case radiation absorption by the crystal lattice, diffractive losses are external with respect to the hot-carrier system.

Let us suppose, for simplicity, that the only mode with a homogeneous distribution of the radiation energy density U is excited inside the resonator. Its amplification is described by the dynamic coefficient of amplification (the dynamic gain):[14,39]

$$\alpha_d(U) = -\frac{\sqrt{\epsilon}}{c}\frac{P_\omega(U)}{U}, \tag{16}$$

where $P_\omega(U)$ is the generated radiation power density. Notice that Eq. (16) is general and holds true for both classical and quantum descriptions of radiation. In the framework of the classical description the radiation energy density U can be written as[14,39]

$$U = \epsilon_0 \epsilon \frac{1}{T_\omega}\int_0^{T_\omega} |E_\omega(t)|^2 dt, \tag{17}$$

where $T_\omega = 2\pi/\omega = 1/f$ is the period of the MW electric field.

The stability of the generation process implies that all radiation losses due to power dissipation inside the system (e.g., power extraction outside the resonator as an output power, etc.) are fully compensated by radiation amplification due to DNDM inside the system. Therefore under stable generation conditions the dynamic gain α_d takes a value of $\alpha_L = \Gamma + \Lambda$ which is equal to the coefficient of the net losses in a resonator, i.e., $\alpha_d(U) = \alpha_L$. The simulation of the nonlinear response allows us to obtain the function $P_\omega(U)$ and to calculate $\alpha_d(U)$ in accordance with Eq. (16). Then, by eliminating U from $P_\omega(U)$ and $\alpha_d(U)$, that is, by expressing P_ω as a function of α_d, one obtains the dependence of the output power for the OPTTR maser on the generalized parameters of the resonator:

$$P_{\mathrm{out}} = P_\omega(\alpha_L)\frac{\Gamma}{\Gamma + \Lambda}. \tag{18}$$

To calculate $P_\omega(U)$ from the MC simulation, it is necessary to take into account the action of the resonant radiation accumulated in the crystal volume on the dynamic motion and the heating of electrons. Hence it is sufficient to introduce the MW electric field of the amplified mode $E_\omega(t) = \mathrm{Re}[E_\omega^0 \exp(i\omega t)]$ directly into the equation of motion $\dot{p}_x(t) = eE_0 + eE_\omega^0 \cos(\omega t)$, which describes the free flight of a trial particle in momentum space. During the simulation of a random trajectory for the single-particle $\mathbf{p}_t$ the time sampling of the average drift velocity is determined by averaging over a large number M of MW electric field periods

$$\langle v(s)\rangle = \frac{1}{M}\sum_{i=0}^{M-1} v_x(\mathbf{p}_{t=s+\mathrm{Ti}}) \tag{19}$$

Downloaded 13 May 2001 to 128.113.4.240. Redistribution subject to AIP license or copyright, see http://ojps.aip.org/japo/japcr.jsp

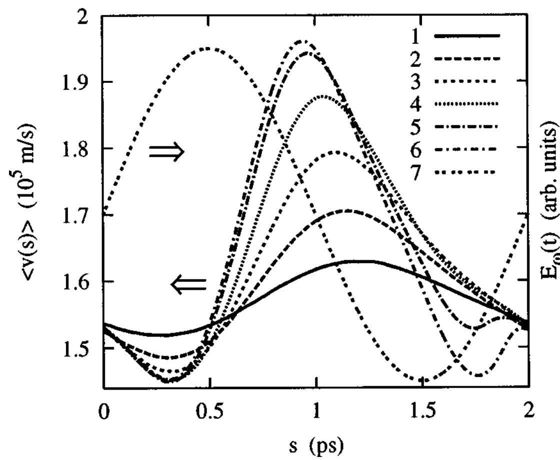

FIG. 10. Velocity response within a period of the MW electric field at a frequency of $f = 0.5$ THz calculated in wurtzite GaN for different amplitudes of the MW field E^0_ω: 0.5, 1, 1.5, 2, 2.5, and 2.7 kV/cm (curves 1–6) with $N_D = 1\times10^{16}\,\mathrm{cm}^{-3}$ at $T_0 = 10$ K. Variations of the MW field are schematically shown by curve 7.

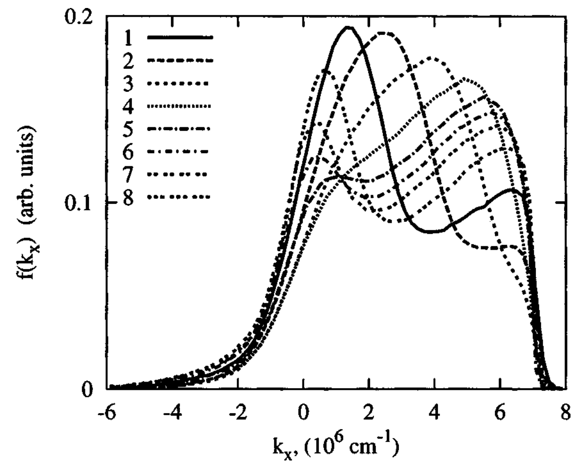

FIG. 11. Instantaneous profiles of the hot-carrier distribution function calculated in wurtzite GaN at different time moments within a period of the MW field. Curves 1–8 correspond to the phase $m\pi/4(m=1,2,...,8)$ of a sinusoidal MW field. Other parameters are $N_D = 1\times10^{16}\,\mathrm{cm}^{-3}$, $T_0 = 10$ K, $E_0 = 2.25$ kV/cm, $E^0_\omega = 1.8$ kV/cm, and $f = 0.5$ THz.

where s belongs to the time interval $0 \leqslant s < T_\omega$. The total power density generated by all carriers is then calculated from its definition as the product of conduction current and applied MW field averaged over the period of oscillation:

$$P_\omega = \frac{en}{T_\omega}\int_0^{T_\omega} \langle v(s)\rangle E_\omega(s)\,ds. \tag{20}$$

According to its definition, P_ω takes negative values in the region of generation and, therefore, the power generated inside the active semiconductor can be given as $P_{\mathrm{gen}} = -P_\omega$.

The procedure described above is used to simulate the nonlinear behavior of a THz maser based on OPTTR. To calculate the velocity response in accordance with Eq. (19), averages of the MW field over $2-8\times10^6$ periods are typically used. As an example, Fig. 10 shows the velocity response to the electric field $E(t) = E_0 + E^0_\omega \sin(\omega t)$ calculated at $f = 0.5$ THz for a wurtzite GaN sample with $N_D = 10^{16}\,\mathrm{cm}^{-3}$ and $T_0 = 10$ K. In accordance with the results of the linear analysis, we choose a constant electric field $E_0 = 2.25$ kV/cm which corresponds to an optimal amplification frequency of about 0.5 THz. Curves 1–6 correspond, respectively, to $E^0_\omega = 0.5$, 1, 1.5, 2, 2.5, and 2.7 kV/cm. The variation of the electric field is shown schematically by curve 7. It is evident that, at least for small amplitudes of the MW field, the main variation of velocity during the MW period is in quadrature with the variation of the electric field. With the increase of the MW field amplitude, the velocity response also increases, but its phase shift with respect to the MW field decreases. This is because of a carrier dynamic bunching in momentum space under resonant interaction at low and intermediate MW field amplitudes[40] (similar to that observed in Refs. 26–28) and its destruction at high amplitudes. This is illustrated by the time evolution of the hot-carrier distribution function $f(k_x, t)$ during a period of the MW field presented in Fig. 11. The order number m of each curve corresponds to a field phase of $m\pi/4$. Quite evident in Fig. 11 are the formation of the electron bunching in the center of the passive region, its further motion across the passive region, and disappearance in the active region.

Figure 12 summarizes the results of the field dependence of the power generated by a single carrier in a wurtzite GaN sample with $N_D = 1\times10^{16}\,\mathrm{cm}^{-3}$ at $T_0 = 10$ K as calculated at frequencies of $f = 0.25$, 0.5, 1, and 1.5 THz with, respectively, the static electric fields of $E_0 = 1.2$, 2.25, 4.3, and 6.35 kV/cm. Each field corresponds to the maximum value of the negative differential mobility at the given frequency. At low MW field amplitudes, the generated power increases first as $|E^0_\omega|^2$, then reaches the maximum values when $E^0_\omega = 0.7-0.9E_0$ and finally decreases to zero when E^0_ω reaches $1-1.2E_0$ at each given frequency. Correspondingly, the dynamical gain is first almost constant and then monotonously decreases to zero. The high values of the optimum amplitude of the MW field lead, in turn, to reasonably high values of

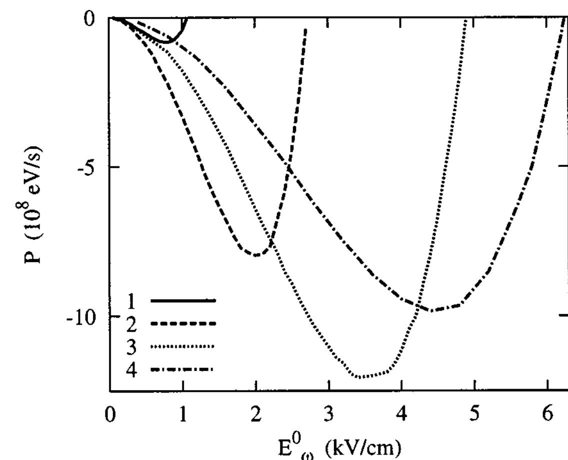

FIG. 12. Power generated at the fundamental frequencies of $f = 0.25$, 0.5, 1, and 1.5 THz (curves 1–4 with, respectively, the static electric fields of $E_0 = 1.2$, 2.25, 4.3, and 6.35 kV/cm) as a function of the amplitude of the MW field calculated in wurtzite GaN with a doping level of $N_D = 1\times10^{16}\,\mathrm{cm}^{-3}$ at $T_0 = 10$ K.

Downloaded 13 May 2001 to 128.113.4.240. Redistribution subject to AIP license or copyright, see http://ojps.aip.org/japo/japcr.jsp

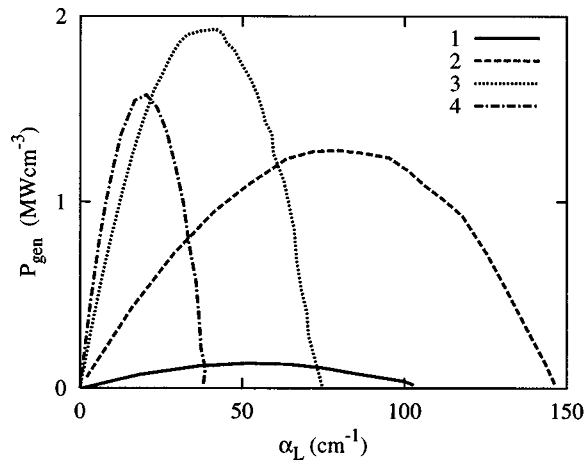

FIG. 13. Power density generated at the fundamental frequencies of $f=0.25$, 0.5, 1, and 1.5 THz (curves 1–4) inside a resonator as a function of the coefficient of total losses inside the resonator, α_L, calculated in wurtzite GaN with a doping level of $N_D=1\times10^{16}\,\mathrm{cm}^{-3}$ at $T_0=10$ K.

the generated power and the generation efficiency, as shown in Figs. 13 and 14 where data are recalculated from that presented in Fig. 12.

Figure 13 shows the generated power density P_{gen} as a function of the net loss coefficient in the resonant system α_L. Let us recall that for a stable generation the dynamical gain must exactly compensate all losses due to power extraction, parasitic, etc., i.e., $\alpha_d=\alpha_L$. Thus if α_L exceeds the static gain given by the linear theory then any stable generation is absent. Therefore with the decrease of α_L at each given frequency the generation starts from the values of the static gain given in Fig. 9. With a further decrease of the net losses, the power increases and reaches a maximum value at the optimum amplitude of the MW field. As follows from Fig. 13, this optimum value is achieved when the dynamical gain is less than its static value by about a factor of 2. With a further decrease of α_L, the amplitude of the MW field increases so considerably that it would destroy the transit-time resonance and carrier bunching. For this reason, the generated power decreases and finally vanishes at $\alpha_L=0$.

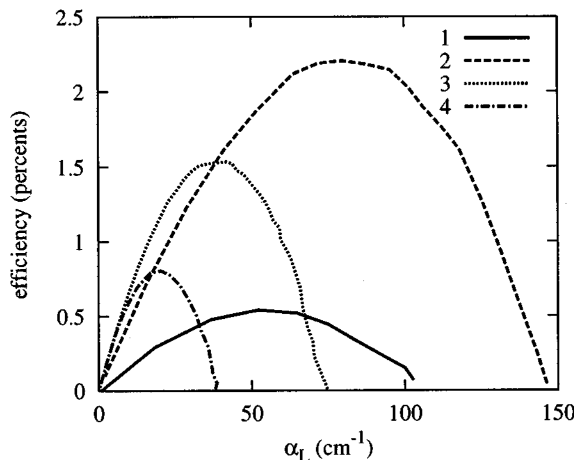

FIG. 14. Efficiency of the power generation at the fundamental frequencies of $f=0.25$, 0.5, 1, and 1.5 THz (curves 1–4) inside a resonator as a function of the coefficient of total losses inside the resonator, α_L, calculated in wurtzite GaN with a doping level of $N_D=1\times10^{16}\,\mathrm{cm}^{-3}$ at $T_0=10$ K.

Figure 14 presents the generation efficiency for the same sample and frequencies of Figs. 12 and 13. During the generation, the average velocity is practically unchanged and merely exhibits a slight increase (up to 1% to 2%) with the increase of E_ω^0 (see Fig. 10). Therefore the maximum values of the efficiency are reached together with the optimum values of the dynamical gain corresponding to the maximum generated power. For the doping level of $N_D=10^{16}\,\mathrm{cm}^{-3}$, see Figs. 12 to 14, the efficiency decreases with the increase in frequency above about 0.5 THz (see curves 2–4 in Fig. 14). This result is associated primarily with the increase of the Joule losses due to the increase in the static electric field E_0. As follows from Figs. 12–14, the chosen impurity concentration $N_D=10^{16}\,\mathrm{cm}^{-3}$ is optimal for power generation at around 0.5 THz, in good agreement with the estimates made by the linear analysis (see Fig. 9). Notice that for the same sample the generation can be achieved in a rather wide frequency range of $f=0.25$–1.5 THz, which is also in a good agreement with the data shown in Fig. 9. For generation frequencies less than 0.5 THz, doping levels less than $N_D=10^{16}\,\mathrm{cm}^{-3}$ are preferable. Correspondingly, for generation at 1 THz and above the optimum impurity concentration is about $N_D=(2-4)\times10^{16}\,\mathrm{cm}^{-3}$, as is also predicted by the linear analysis.

VI. CONCLUSIONS

Both linear and nonlinear studies of the optical phonon transit-time resonance (OPTTR) have been carried out at temperatures up to 80 K in bulk zinc blende and wurtzite GaN. Results show that GaN is a promising material for THz power generation. It should be underlined that the instability considered above is not related with any space-charge effects and corresponds to amplification or generation of the transverse electromagnetic waves propagating in a homogeneous active medium. In such a case, generation is usually achieved experimentally in bulk samples whose dimensions in the direction of wave propagation are greater than the wavelength of generated radiation. In so doing, the role of a resonant system is often played by the sample surfaces perpendicular to the direction of wave propagation.[14,15,20,21] Since the frequency range of the GaN OPTTR maser amplification is similar to that of the inter-valence-band germanium laser[15] one can expect that in the THz region the optimal sizes of a sample and the kind of the resonant system can be similar to those of the *p*-Ge THz laser working at the same frequency. Moreover, due to a high value of the amplification coefficient, the sample sizes of the GaN OPTTR maser can be additionally decreased. By comparing the characteristics of power generation identified in this investigation with those of similar devices experimentally realized up-to-date, namely, the 0.04–0.33 THz negative mass cyclotron resonance maser[21] and the 1–4 THz inter-valence-band germanium laser,[14,15] the OPTTR GaN maser offers the following advantages: (i) a wider tuning range of working temperatures also including the liquid nitrogen temperature, (ii) a much higher value of the maximum amplification coefficient (100

Downloaded 13 May 2001 to 128.113.4.240. Redistribution subject to AIP license or copyright, see http://ojps.aip.org/japo/japcr.jsp

cm^{-1} for the OPTTR maser versus 1 and 0.1 cm^{-1} for the cyclotron resonance maser and germanium laser, respectively), (iii) a wider tuning range of frequency, covering the whole submillimeter range ($f = 0.3–3$ THz), obtainable by using only an applied electric field, (iv) the absence of a magnetic field, which simplifies the device design, the power extraction, etc., and (v) a very narrow amplification band with high absorption coefficient outside the band, useful for realizing the single-mode generation.

The difference in OPTTR characteristics for the zinc blende and wurtzite modifications is mainly related to the difference in the effective mass (0.15 and 0.2, respectively) and the difference usually does not exceed 20%. For example, to obtain the same generation frequency, the required static electric field in wurtzite GaN is about 20% higher than in zinc blende GaN.

The thermal effects (i.e., heating of the sample during the power generation) for the maser proposed here are largely caused by optical phonon emissions and are, to some extent, similar to those found in the cyclotron resonance maser and germanium laser. Therefore the experimental realization of the latter two devices and the OPTTR maser in *n*-InP[20] combined with the encouraging results presented in this article should provide a solid foundation for experimentalists to demonstrate the OPTTR THz GaN maser described in this article.

ACKNOWLEDGMENTS

The authors wish to acknowledge the support of the NATO collaborative-linkage grant PST.CLG.976340, the high-level grant DRB4/MDL/no 99-30 of the french *Ministere de l'Education nationale, de la recherche et de la technologie*, the french-lithuanian bilateral cooperation n. 5380 of french CNRS, MADESS II project of the Italian Consiglio Nazionale delle Ricerche (CNR), and the CAIP center of Rutgers University.

[1] *New Directions in Terahertz Technology*, edited by J. M. Chamberlain and R. E. Miles (Kluwer, Dordrecht, 1997).
[2] R. Kamoua, H. Eisele, and G. I. Haddad, Solid-State Electron. **36**, 1547 (1993).
[3] M. F. Zybura, S. H. Jones, B. W. Lim, J. D. Crowley, and J. E. Carlstrom, Solid-State Electron. **39**, 547 (1996).
[4] C. Benz and J. Freyer, Electron. Lett. **34**, 2351 (1999).
[5] T. W. Crowe, Int. J. Infrared Millim. Waves **10**, 765 (1989).
[6] V. Gruzhinskis, E. Starikov, P. Shiktorov, L. Reggiani, M. Saraniti, and L. Varani, Appl. Phys. Lett. **61**, 1456 (1992).
[7] T. C. L. G. Sollner, W. D. Goodhue, P. E. Tannenwald, C. D. Parker, and D. D. Peck, Appl. Phys. Lett. **43**, 588 (1983).
[8] H. Drexler, J. S. Scott, S. J. Allen, K. L. Campman, and A. G. Gossard, Appl. Phys. Lett. **67**, 2816 (1995).
[9] Z. S. Gribnikov, A. N. Korshak, and N. Z. Vagidov, J. Appl. Phys. **80**, 5799 (1996).
[10] M. Dyakonov and M. Shur, Phys. Rev. Lett. **71**, 2465 (1993).
[11] K. Kempa, P. Bakshi, and E. Gornik, Phys. Rev. B **54**, 8231 (1996).
[12] P. Shiktorov, V. Gružinskis, E. Starikov, L. Reggiani, and L. Varani, Semicond. Sci. Technol. **12**, 1331 (1997).
[13] E. R. Brown, W. D. Goodhue, and T. C. L. G. Sollner, J. Appl. Phys. **64**, 1519 (1988).
[14] Special issue on Far-infrared Semiconductor Lasers, edited by E. Gornik and A. A. Andronov, [Opt. Quantum Electron. **23**, S111 (1991)].
[15] E. Brundermann, D. R. Chamberlin, and E. E. Haller, Appl. Phys. Lett. **73**, 2757 (1998).
[16] Yu. K. Pozhela, E. V. Starikov, and P. N. Shiktorov, Phys. Status Solidi B **128**, 653 (1985).
[17] E. V. Starikov and P. N. Shiktorov, Sov. Phys. Semicond. **17**, 1355 (1983).
[18] Yu. K. Pozhela, E. V. Starikov, and P. N. Shiktorov, Semicond. Sci. Technol. **7**, B386 (1992).
[19] E. V. Starikov and P. N. Shiktorov, Liet. Fiz. rinkinis **32**, 471 (1992).
[20] L. E. Vorob'ev, S. N. Danilov, Yu. V. Kochegarov, V. N. Tulupenko, and D. A. Firsov, in Abstracts of IVth Russian Conference on the Physics of Semiconductors, 1999, Novosibirsk, p. 42.
[21] V. I. Gavrilenko and Z. F. Krasil'nik, Opt. Quantum Electron. **23**, S323 (1991).
[22] E. V. Starikov and P. N. Shiktorov, Opt. Quantum Electron. **23**, S341 (1991).
[23] W. Fawcett, A. D. Boardman, and S. Swain, J. Phys. Chem. Solids **31**, 1963 (1970).
[24] I. I. Vosilius and I. B. Levinson, Sov. Phys. JETP **23**, 1104 (1966); **25**, 672 (1967).
[25] S. Komiyama, Adv. Phys. **31**, 255 (1982).
[26] P. N. Shiktorov, Sov. Phys. Collect. **25**, 59 (1985).
[27] T. Kurosawa and Y. Kosano, Jpn. J. Appl. Phys., Part 1 **58**, 4104 (1989).
[28] N. Ishida and T. Kurosawa, Jpn. J. Appl. Phys., Part 1 **64**, 2994 (1995).
[29] A. Matulionis, J. Pozhela, and A. Reklaitis, Phys. Status Solidi A **31**, 83 (1975).
[30] V. Bareikis, A. Galdikas, R. Miliushyte, J. Pozhela, and V. Viktoravichius, J. Phys. (France) **42**, C7-215 (1981); **42**, C7-215-220 (1981).
[31] A. A. Andronov and V. A. Kozlov, Pis'ma Zh. Eksp. Teor. Fiz. **17**, 124 (1973).
[32] Ya. I. Alber, A. A. Andronov, V. A. Valov, V. A. Kozlov, A. M. Lerner, and I. P. Rumyantseva, Zh. Eksp. Teor. Fiz. **72**, 1030 (1977).
[33] Yu. V. Gulyaev and I. I. Chusov, Fiz. Tverd. Tela (Leningrad) **20**, 2637 (1978).
[34] A. Matulis and A. Chenis, Sov. Phys. JETP **50**, 572 (1979).
[35] P. J. Price, J. Appl. Phys. **53**, 8805 (1982).
[36] P. J. Price, J. Appl. Phys. **54**, 3616 (1983).
[37] B. E. Foutz, L. F. Eastman, U. V. Bhapkar, and M. S. Shur, Appl. Phys. Lett. **70**, 2849 (1997).
[38] J. D. Albrecht, R. P. Wang, P. P. Ruden, M. Farahmand, and K. F. Brennan, J. Appl. Phys. **83**, 4777 (1998).
[39] A. Yariv, *Quantum Electronics*, 2nd ed. (Wiley, New York, 1975).
[40] A. Matulis and A. Chenis, Sov. Phys. JETP **57**, 927 (1983).

Downloaded 13 May 2001 to 128.113.4.240. Redistribution subject to AIP license or copyright, see http://ojps.aip.org/japo/japcr.jsp